Chemical Science

ROYAL SOCIETY OF CHEMISTRY

EDGE ARTICLE

View Article Online
View Journal | View Issue

Cite this: *Chem. Sci.*, 2025, **16**, 18390

All publication charges for this article have been paid for by the Royal Society of Chemistry

Reticular chemistry guided construction of Olympic rings-inspired two-dimensional covalent organic frameworks for photocatalysis

Ze-Yang Wang, Chao-Qin Han, Jia-Xin Guo, Shuai Sun and Xiao-Yuan Liu *

Two-dimensional covalent organic frameworks (2D-COFs) have received extensive attention from structural design to application explorations. Top-down design and discovery of new structures of 2D-COFs still remains a great challenge. In this work, under the guidance of reticular chemistry, we rationally designed and synthesized four highly crystalline 2D-COFs (HIAM-0028 to HIAM-0031) inspired by the Olympic rings using hexatopic aldehydes and diamine-based building units through a $C_6 + C_2$ approach. Due to their capacity to generate reactive oxygen species and suitable electronic structures, these COFs can be used as heterogeneous photocatalysts for the cycloaddition reaction of tertiary anilines and maleimides. HIAM-0030 exhibits the best photocatalytic performance and can be used to synthesize the target compound on a gram scale with a yield of >93%, which is attributed to its lower exciton binding energy, efficient separation and migration of photogenerated charges. This work represents a great example of building COFs with unique structures guided by reticular chemistry and provides a class of efficient photocatalysts for organic transformation.

Received 30th May 2025
Accepted 26th August 2025

DOI: 10.1039/d5sc03939h

rsc.li/chemical-science

Introduction

Porous materials, especially metal–organic frameworks (MOFs)[1] and covalent organic frameworks (COFs),[2–4] have received extensive attention in the past two decades. Due to their intrinsic porosity, tunable structures, compositions and functionalities, MOFs and COFs have been widely explored for potential applications in chemical separation and storage,[5,6] catalysis[7–10] and biorelated areas.[11–13] To realize on-demand properties with well-defined structures and functionalities, it is essential to develop a tool for the rational design and preparation of porous materials. The establishment and development of reticular chemistry[14–16] and the Reticular Chemistry Structure Resource (RCSR) database[17] shed light on the top-down design and precise assembly of porous materials at the molecular level using rationally designed building units.[18–22] Guided by reticular chemistry, numerous MOFs and COFs have been constructed with customized structures[23–35] and enhanced performances.[36–39]

Under the guidance of reticular chemistry, Olympic rings-inspired MOFs were successfully constructed,[28] which exhibit great stability and tunable emission properties. As depicted in Scheme 1a, to satisfy the periodicity requirement for crystalline materials, we have to remove the rings to form fused five-member rings, after which the two-dimensional (2D) structure can be generated. For the construction of the inspired three-dimensional (3D) MOFs, the great challenge is to build the 3D structure from the 2D structure and derive the structure of organic linkers (Scheme 1b). However, for the construction of COFs, especially for 2D-COFs, it is much easier to propose the organic building units than for 3D-MOFs using the fused Olympic rings. As illustrated in Scheme 1c, Olympic rings-inspired 2D-COFs might be synthesized by the combination of C_6-symmetric and C_2-symmetric linkers.

Benefiting from the unlimited organic building units and tunable functionalities, COFs exhibit great potential as photocatalysts for photocatalytic water splitting, CO_2 reduction, H_2O_2 generation and organic transformation.[7,8,40–44] Since the report of oxidative hydroxylation of arylboronic acids to phenols using benzoxazole-linked COFs,[45] COF-based photocatalytic organic transformations have generated great interest. To date, COFs have been used to catalyze a wide range of organic reactions, including but not limited to aerobic oxidation of sulfides,[46] oxidative coupling of amines,[47] C–H borylation and functionalization.[48–51]

Herein, the use of reticular chemistry, as discussed above, enabled us to construct four Olympic rings-inspired 2D COFs, HIAM-0028 to HIAM-0031 (HIAM stands for Hoffmann Institute of Advanced Materials), using hexatopic aldehydes and diamine-based building units. These COFs exhibit high crystallinity and can serve as promising photocatalysts for the photocatalytic cycloaddition reaction of tertiary anilines and maleimides due to their suitable electronic structures and the capacity to generate reactive oxygen species. Among these COFs,

Hoffmann Institute of Advanced Materials, Shenzhen Polytechnic University, 7098 Liuxian Blvd, Nanshan District, Shenzhen, 518055, P. R. China. E-mail: liuxiaoyuan1989@szpu.edu.cn

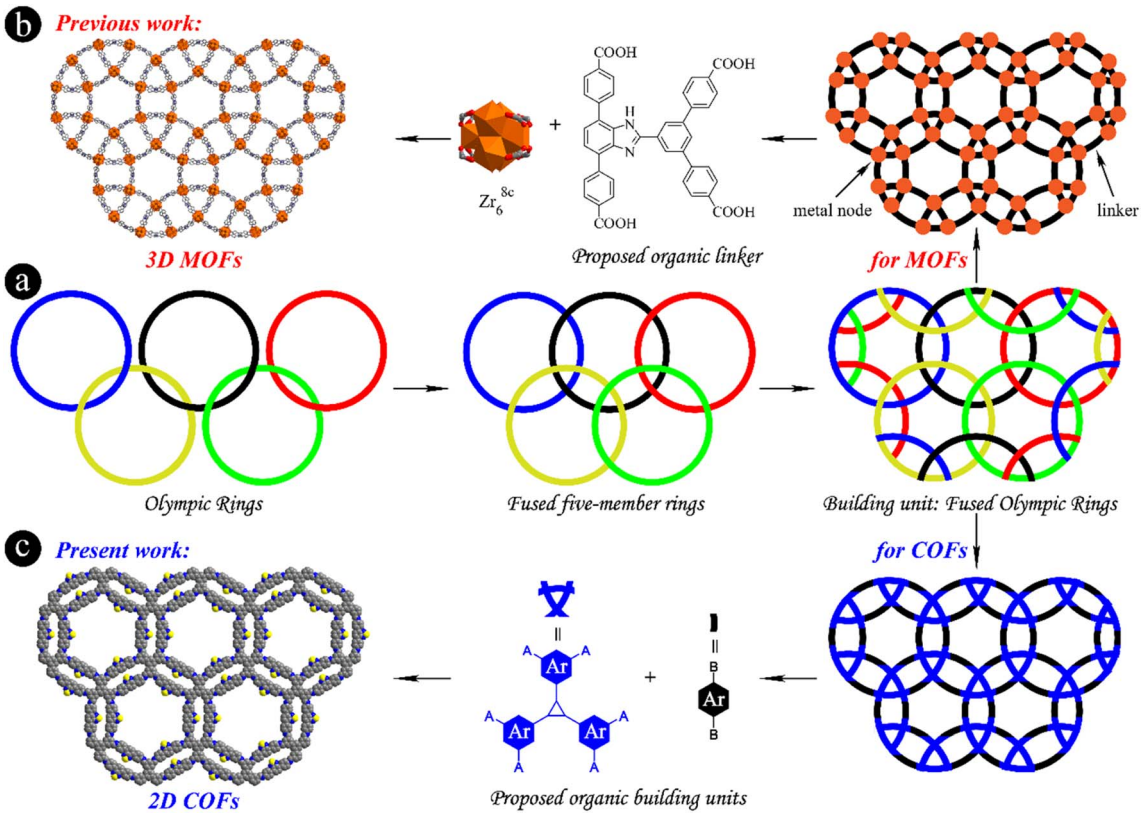

Scheme 1 The schematic diagram illustrating the rational design and construction of the Olympic rings-inspired porous material. (a) The generation of ordered patterns from the Olympic rings; (b) the Olympic rings-inspired 3D zirconium-based MOFs, single-crystal structures and the corresponding organic linker; (c) the Olympic rings-inspired 2D COFs and the proposed structures of organic building units. The permission has been obtained for the use of Olympic Properties from the International Olympic Committee.

HIAM-0030 possesses lower exciton binding energy, efficient separation and migration of electron–hole pairs, leading to the highest photocatalytic performance.

Results and discussion

Based on the aforementioned discussion and proposed $C_6 + C_2$ organic building units, 5′-(3,5-diformylphenyl)-[1,1′ : 3′,1″-terphenyl]-3,3″,5,5″-tetracarbaldehyde (DPTTA) and 4,4′-(benzo[*c*][1,2,5]thiadiazole-4,7-diyl)dianiline (BTDA) were chosen as the hexa-aldehyde and diamine to construct the 2D-COF and verify our hypothesis (Fig. 1a1). By condensing DPTTA and BTDA with a molar ratio of 1 : 3 in a mixture solution of *n*-butyl alcohol/*o*-dichlorobenzene/6 M acetic acid with a volume ratio of 5 : 5 : 1 at 120 °C for 3 days, a yellow powder of HIAM-0028 was obtained. Fourier transform infrared (FT-IR) spectroscopy and solid-state ^{13}C nuclear magnetic resonance (^{13}C-NMR) were employed to examine the formation of imine bonds between DPTTA and BTDA after the reaction. As shown in Fig. 2a and S1, HIAM-0028 exhibits a strong C=N stretching vibration at 1622 cm^{-1}, accompanied by the disappearance of the C=O bond at 1700 cm^{-1} in DPTTA and the N–H stretch in the range of 3312–3407 cm^{-1}. The ^{13}C-NMR spectrum of HIAM-0028 exhibits the characteristic carbon peaks of the carbon atom of the imine bond at 159 ppm (Fig. 2b).

Then the crystal structure of HIAM-0028 was analyzed by powder X-ray diffraction (PXRD) experiment and simulation calculation. As shown in Fig. 1a2 and a3, the Olympic rings-inspired structure of HIAM-0028 was obtained, which exhibited distinct diffraction peaks at 2.26°, 3.87° and 4.52°, corresponding to the (100), (102), and (200) lattice planes, respectively. These experimental PXRD patterns are well-aligned with the simulated diffraction peaks based on the AA-or AB-stacking model (Fig. 1a3 and S2). The Rietveld refinement results revealed very small discrepancies with the good agreement factor of $R_p = 5.19\%$ and $R_{wp} = 2.53\%$ for HIAM-0028. The unit cell parameters of HIAM-0028 were determined as follows: $a =$ 45.55 Å, $b = 3.45$ Å, $c = 45.53$ Å, $\alpha = \gamma = 90°$, $\beta = 121.03°$ for HIAM-0028 (Table S1). The morphology, crystallinity and compositions of HIAM-0028 were evidenced by scanning electron microscope (SEM), transmission electron microscope (TEM) and energy-dispersive X-ray (EDX) analysis. HIAM-0028 has a rod-like morphology with homogeneous distributions of C, N and S elements (Fig. S3 and S4). Clear lattice fringes were observed for HIAM-0028 using high-resolution TEM (Fig. S5). The distance between the one-dimensional lattice fringes is about 3.60 nm for HIAM-0028, which is close to the theoretical distance between the hexagonal pores, which confirms the AA-stacking structure of HIAM-0028. The aforementioned results demonstrate that the Olympic rings-inspired 2D-COF indeed

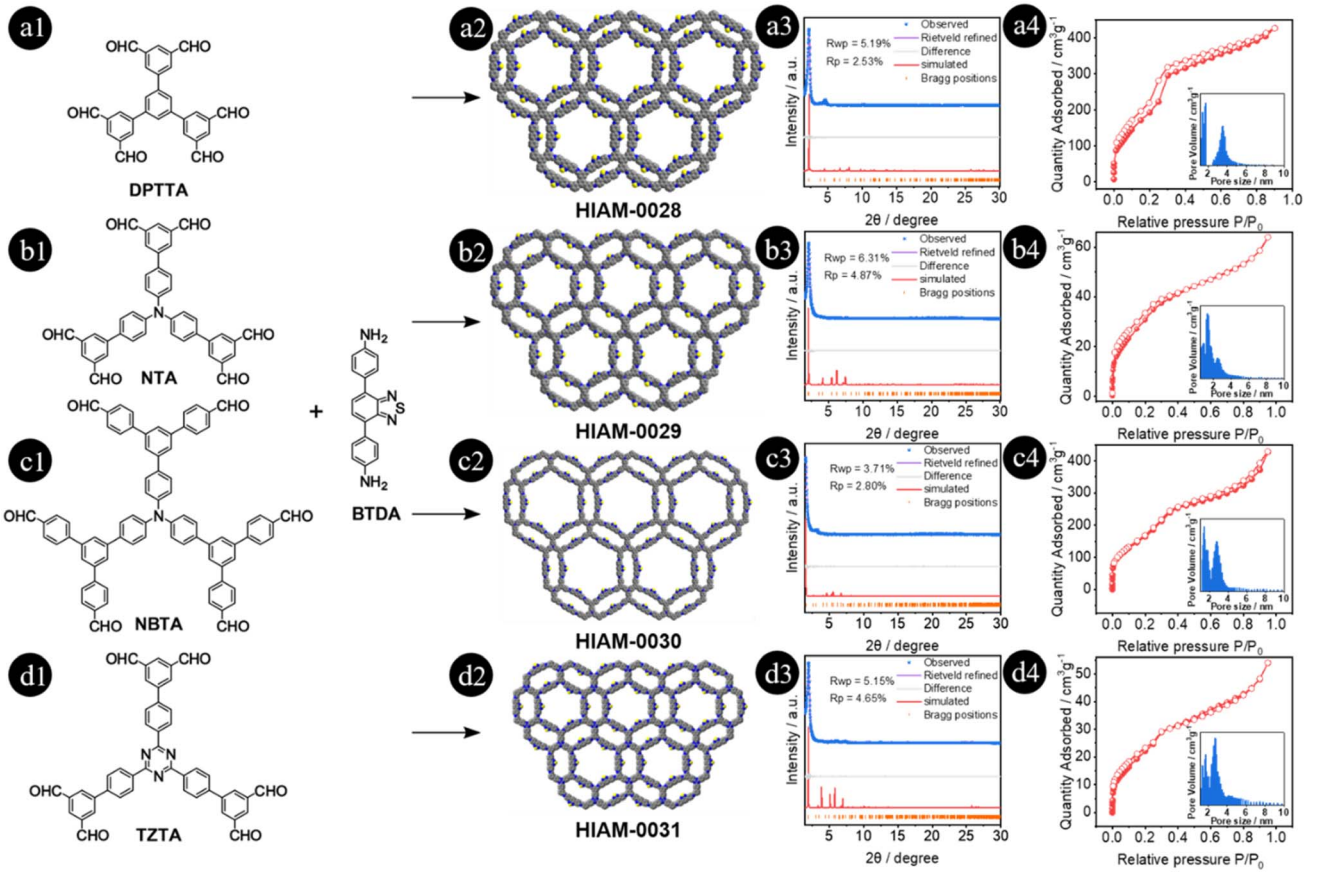

Fig. 1 Structures of organic building units and the characterization studies of corresponding COFs (HIAM-0028, HIAM-0029, HIAM-0030 and HIAM-0031). The structures of hexa-aldehydes of DPTTA (a1), NTA(b1), NBTA (c1) and TZTA (d1); the structures of HIAM-0028 (a2), HIAM-0029 (b2), HIAM-0030 (c2) and HIAM-0031 (d2); the experimental and simulated PXRD patterns (based on the AA-stacking model) of HIAM-0028 (a3), HIAM-0029 (b3), HIAM-0030 (c3) and HIAM-0031 (d3); the N_2 adsorption–desorption isotherms and corresponding pore size distributions of HIAM-0028 (a4), HIAM-0029 (b4), HIAM-0030 (c4) and HIAM-0031 (d4) at 77 K.

can be constructed with high crystallinity *via* insightful structural pre-analysis and judicious choice of organic building units.

Based on the above results, other three hexa-aldehydes, namely 4′,4″,4‴-nitrilotribiphenyl-3,5-dicarbaldehyde (NTA), 5′,5‴′,5‴′′′-(nitrilotris(benzene-4,1-diyl))tris(([1‴,1‴′:3‴′,1‴′′-terphenyl]-4,4″-dicarbaldehyde)) (NBTA) and 4′,4‴,4‴′′–(1,3,5-triazine-2,4,6-triyl)tris(([1,1′-biphenyl]-3,5-dicarbaldehyde)) (TZTA) (Fig. 1b1–d1), were used to evaluate the universality and linker adaptability of this reticular chemistry guided top-down design principle. The corresponding COFs, HIAM-0029, HIAM-0030 and HIAM-0031, were synthesized using a similar method to that of HIAM-0028. The formation of imine bonds in these three COFs was confirmed by FTIR and ^{13}C-NMR (Fig. 2a, b and S1). The crystal structures of HIAM-0029, HIAM-0030 and HIAM-0031 were also analyzed by PXRD experiments and simulation calculations (Fig. 1b2–d3). The PXRD measurement of HIAM-0029 revealed high crystallinity with characteristic peaks at 2.06°, 4.13° and 5.41°, corresponding to the (110), (220), and (310) facets, respectively. HIAM-0030 showed a sharp peak at a low angle of 1.53° and a weaker diffraction peak at 2.68°, which were derived from (110) and (120) Bragg planes, respectively. The PXRD patterns of HIAM-0031 displayed diffraction peaks at 2θ of 1.99°, 3.40° and 3.98°, which can be attributed to the (100), (210), and (200) reflections, respectively. These PXRD patterns showed excellent agreement with the simulated diffraction peaks based on the AA- or AB-stacking model (Fig. 1b3, c3, d3 and S2). The Rietveld refinement results revealed very small discrepancies with a good agreement factor of R_p = 6.31% and R_{wp} = 4.87% for HIAM-0029; R_p = 3.71% and R_{wp} = 2.80% for HIAM-0030; R_p = 5.15% and R_{wp} = 4.65% for HIAM-0031. The unit cell parameters of these three COFs were determined as follows: a = 49.65 Å, b = 49.48 Å, c = 3.81 Å, $\alpha = \beta = 90°$, $\gamma = 119.17°$ for HIAM-0029; a = 65.07 Å, b = 67.40 Å, c = 3.37 Å, $\alpha = \beta = 90°$, $\gamma = 120.41°$ for HIAM-0030; a = 51.86 Å, b = 50.59 Å, c = 3.41 Å, $\alpha = \beta = 90°$, $\gamma = 58.61°$ for HIAM-0031 as summarized in Tables S2–S4. The morphology, crystallinity and composition of HIAM-0029, HIAM-0030 and HIAM-0031 were also examined using SEM, TEM and EDS (Fig. S3, S5–S8).

Then the porosity of these four COFs was evaluated through nitrogen adsorption–desorption at 77 K, which can be utilized to further confirm the structures of these four COFs. As depicted in Fig. 1a4–d4, all of the COFs showed type IV isotherms, which

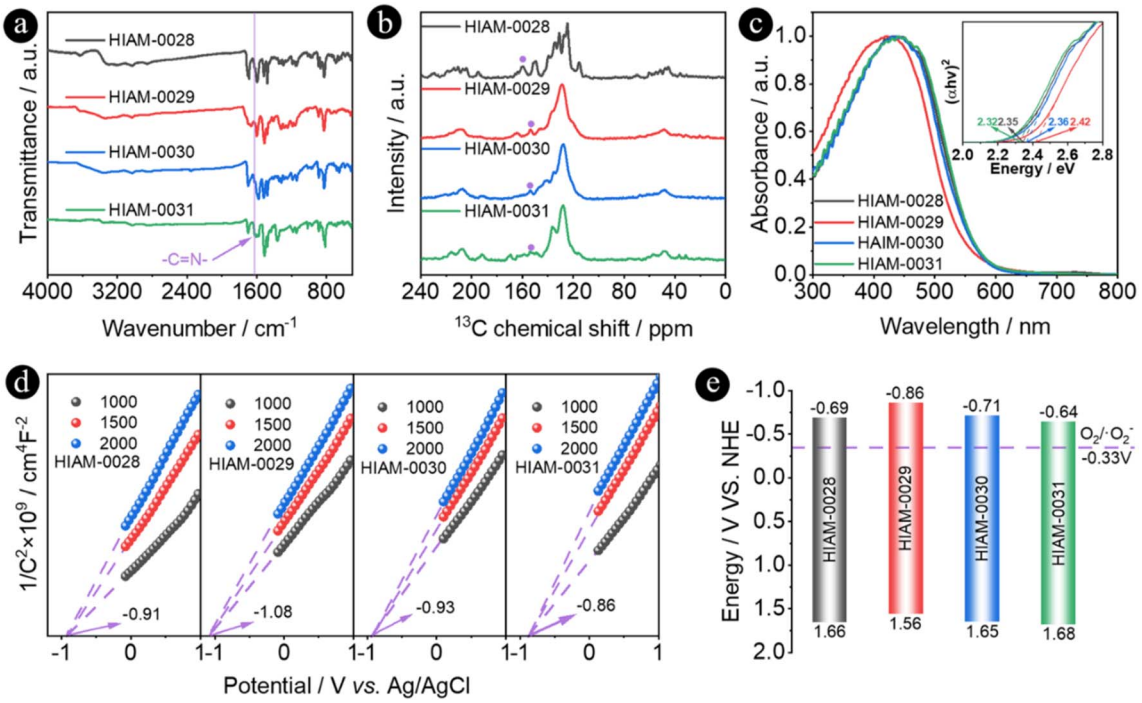

Fig. 2 The FT-IR spectra (a), ^{13}C-NMR spectra (b), normalized UV-vis diffuse reflection absorption spectra and the corresponding Tauc plots (c), Mott–Schottky plots at different frequencies (d), and energy band structures (e) of HIAM-0028, HIAM-0029, HIAM-0030 and HIAM-0031.

are characteristic of microporous and mesoporous materials. The Brunauer–Emmett–Teller (BET) surface areas of HIAM-0028, HIAM-0029, HIAM-0030 and HIAM-0031 were measured to be 811.3, 151.2, 650.4 and 78.4 $m^2 g^{-1}$, respectively. The pore size distributions were calculated to be approximately 1.43, 1.78 and 3.55 nm for HIAM-0028; 0.89, 1.94 and 2.53 nm for HIAM-0029; 1.41, 1.68 and 2.77 nm for HIAM-0030; 1.41, 1.71 and 2.76 nm for HIAM-0031 using non-local density functional

Table 1 Control experiments of the cycloaddition reaction of *N*,*N*,4-trimethylaniline and 1-phenylpyrrolidine-2,5-dione. Reaction conditions: *N*,*N*,4-trimethylaniline (0.50 mmol), 1-phenylpyrrolidine-2,5-dione (0.25 mmol) and 5.0 mg COFs in 3.0 mL DMF under air with the irradiation of a 40 W white light LED at room temperature (R.T.)

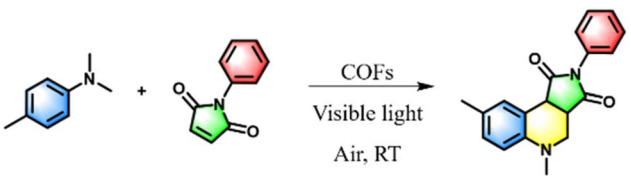

Entry	Catalyst	Light	Air	Additive	Time (h)	Conversion[a] (%)
1	HIAM-0028	On	+	—	18	57
2	HIAM-0029	On	+	—	18	98
3	HIAM-0029	On	+	—	14	70
4	HIAM-0030	On	+	—	18	99
5	HIAM-0030	On	+	—	14	90
6	HIAM-0031	On	+	—	18	70
7	HIAM-0030	Off	+	—	18	Trace
8	HIAM-0030	On	–	—	18	Trace
9	HIAM-0030	On	+	Benzoquinone	18	15
10	HIAM-0030	On	+	L-Histidine	18	99
11	HIAM-0030	On	+	Isopropanol	18	99
12	HIAM-0030	On	+	$AgNO_3$	18	50
13	HIAM-0030	On	+	KI	18	Trace

[a] Determined by GC-MS

theory (NLDFT), suggesting the AA-stacking model for HIAM-0028 to HIAM-0031. Then the thermal and chemical stabilities for HIAM-0028 to HIAM-0031 were evaluated. As shown in Fig. S9, the thermogravimetric analysis (TGA) indicated that four COFs exhibit high thermal stability up to 400 °C. The four COFs were treated under various conditions to test their chemical stability, including water, boiling water, pH = 2, 4, 10 and 12 solutions for 24 hours. The observed C=N stretching vibrations (Fig. S10) and well-matched PXRD patterns (Fig. S11) for COFs before and after treatments demonstrated the high chemical stabilities of HIAM-0028 to HIAM-0031.

To achieve efficient photocatalysis, the light-harvesting capacity is one of the important parameters for photocatalysts. Therefore, the solid-state UV-vis absorption spectra were recorded to investigate the light-harvesting capacity of these COFs, which is important for their photocatalysis. As shown in Fig. 2c, HIAM-0028, HIAM-0030 and HIAM-0031 exhibit almost the same absorption spectra, while a slight blue shift was observed for HIAM-0029. According to Tauc's plots derived from the UV-vis spectra, the band gaps (E_g) were determined to be 2.35, 2.42, 2.36 and 2.32 eV for HIAM-0028, HIAM-0029, HIAM-0030 and HIAM-0031, respectively (Fig. 2c inset). Then from the Mott–Schottky experiments, the conduction band (E_{CB}) of HIAM-0028, HIAM-0029, HIAM-0030 and HIAM-0031 was obtained as −0.91, −1.08, −0.93 and −0.86 V (*vs.* Ag/AgCl), respectively (Fig. 2d). Based on E_g and E_{CB}, the valence band (E_{VB}) of HIAM-0028, HIAM-0029, HIAM-0030 and HIAM-0031 is calculated to be 1.66, 1.56, 1.65 and 1.68 (*vs.* the normal hydrogen electrode), respectively (Fig. 2e). These results indicated that these four COFs possess sufficient band structures for the generation of superoxide radical anion ($^{\bullet}O_2^-$) from O_2, which is one of important reactive oxygen species for photocatalytic aerobic oxidation reactions.

Bearing the aforementioned results in mind, the cycloaddition reaction of tertiary aniline and maleimide to synthesize 1,2,3,4-tetrahydroquinoline-based products was employed as a representative reaction to investigate the applicability of these four COFs for photocatalytic oxidative reactions.[52] As shown in Table 1, a typical procedure for the photocatalytic reaction is as follows: *N*,*N*,4-trimethylaniline (0.50 mmol), 1-phenylpyrrolidine-2,5-dione (0.25 mmol), and COFs as the photocatalyst (5.0 mg) were added into a reactor containing 3.0 mL *N*,*N*-dimethylformamide (DMF), which was irradiated using a 40 W white LED lamp at room temperature under air. After 18 hours, the conversion to generate 5,8-dimethyl-2-phenyl-3*a*,4,5,9*b*-tetrahydro-1*H*-pyrrolo[3,4-*c*]quinoline-1,3(2*H*)-dione was 57%, 98%, 99% and 70% for HIAM-0028, HIAM-0029, HIAM-0030 and HIAM-0031, respectively (Table 1, entries 1, 2, 4 and 6). When the reaction time was reduced to 14 hours, the conversions were 70% and 90% for HIAM-0029 and HIAM-0030 (Table 1, entries 3 and 5). These results indicate that the order of the photocatalytic activities of these COFs is HIAM-0030 > HIAM-0029 > HIAM-0031 > HIAM-0028. The photocatalytic performance of HIAM-0030 is higher than or comparable with these reported COF-based photocatalysts for the synthesis of tetrahydroquinoline, as summarized in Table S5.[52–56]

To investigate the different photocatalytic performances of these four COFs, their transient photocurrent responses

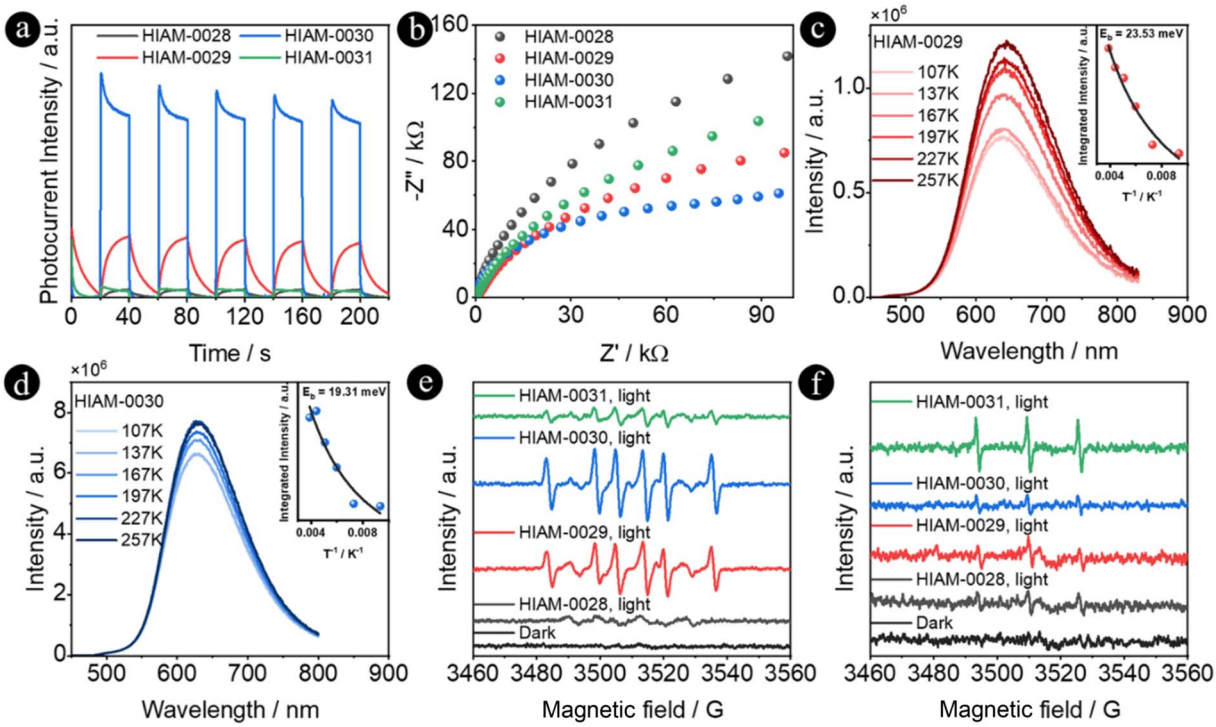

Fig. 3 The transient photocurrent responses (a) and ESI Nyquist plots (b) of HIAM-0028, HIAM-0029, HIAM-0030 and HIAM-0031; the temperature-dependent photoluminescence spectra and their corresponding exciton binding energy of HIAM-0029 (c) and HIAM-0030 (d); EPR detection of $^{\bullet}O_2^-$ (e) and $^1O_2$ (f) for HIAM-0028, HIAM-0029, HIAM-0030 and HIAM-0031.

(Fig. 3a) and electronical impedance spectra (EIS) (Fig. 3b) were measured. Compared with HIAM-0028, HIAM-0029 and HIAM-0031, HIAM-0030 exhibited a higher photocurrent response intensity and a lower charge transfer resistance, suggesting its superior electron–hole separation efficiency and interfacial charge migration capability. Furthermore, the temperature-dependent photoluminescence spectra of these four COFs were measured to further investigate the separation and recombination characteristics of the electron–hole pairs. As shown in Fig. 3c, d and S12, gradually enhanced emission intensities were recorded for four COFs with rising temperatures. Accordingly, the exciton binding energy (E_b) values were found to be 25.86, 23.53, 19.31 and 41.70 meV for HIAM-0028, HIAM-0029, HIAM-0030 and HIAM-0031, respectively, based on the Arrhenius equation $[I(T) = I_0/(1 + A\exp(-E_b/k_bT)]$ to fit the plot of integrated emission spectra as a function of $1/T$ at different temperatures (Fig. 3c, d and S8 inset). This result further demonstrates that HIAM-0030 has the most efficient electron–hole separation to facilitate photocatalysis.

Then a series of control experiments were carried out to examine the key intermediate in the photocatalytic reaction. As shown in Table 1, entries 7 and 8, almost no product was detected in the absence of light and air, indicating light and O_2 are the essential elements to trigger this reaction. When benzoquinone, the $^{\bullet}O_2^-$ scavenger, was added to the reaction, the conversion significantly reduced to 15%, which suggests that $^{\bullet}O_2^-$ is the predominant radical in this reaction (Table 1, entry 9). No changes were observed in the reaction conversion upon addition of L-histidine ($^1O_2$ scavenger) and isopropanol ($^{\bullet}OH$ scavenger), ruling out the effect from $^1O_2$ and $^{\bullet}OH$ in the reaction (Table 1, entries 10 and 11). In addition, the addition of $AgNO_3$ as the electron scavenger and KI as the hole scavenger can also remarkably quench the reaction, revealing that photogenerated electrons and holes are essential for the photocatalytic reaction (Table 1, entries 12 and 13). Then, to confirm the generation of $^{\bullet}O_2^-$ using these COFs, the electron paramagnetic resonance (EPR) measurements were performed using 5,5-dimethyl-1-pyrroline-*N*-oxide (DMPO) as the trapping agent. As shown in Fig. 3e, obvious and characteristic signals belonging to DMPO-$^{\bullet}O_2^-$ were recorded for HIAM-0028 to HIAM-0031 under irradiation. It should be noted that HIAM-0030 exhibits the highest intensity, which is also consistent

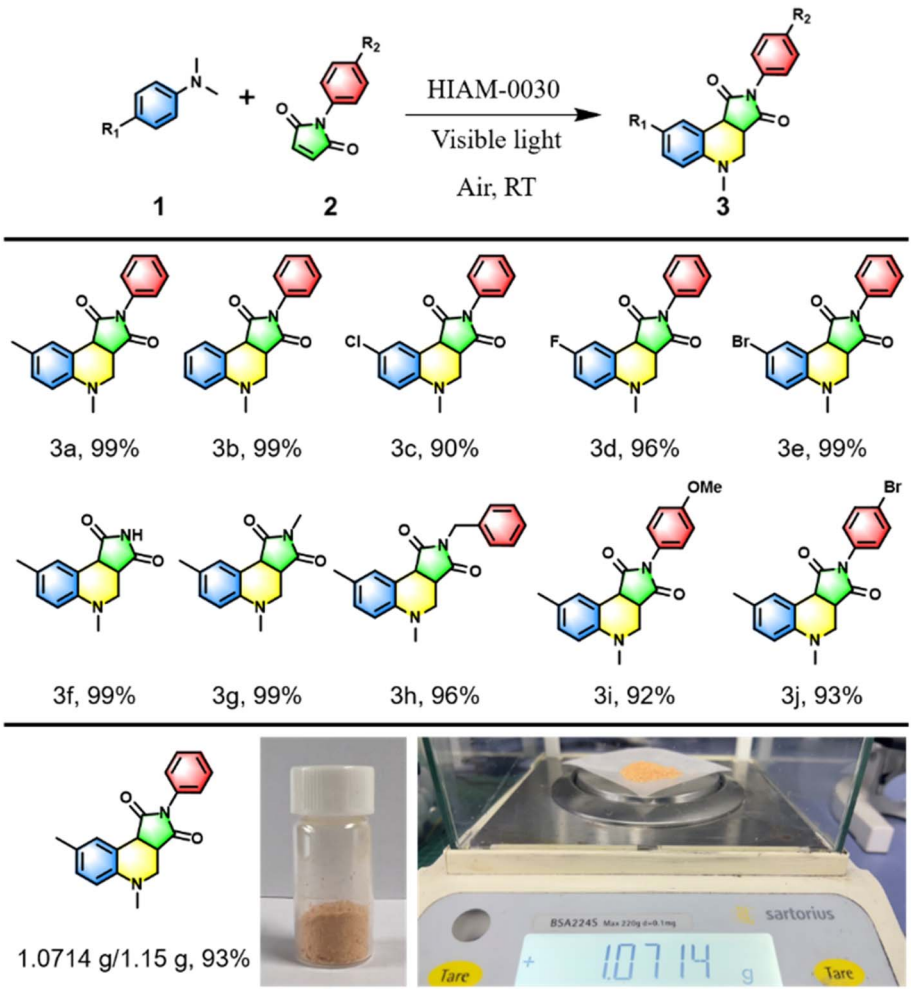

Fig. 4 Substrate extension of the cycloaddition reaction of various tertiary anilines and maleimides (reaction conditions: 0.50 mmol tertiary anilines, 0.25 mmol maleimides and 5.0 mg HIAM-0030 in 3.0 mL DMF under air with the irradiation of a 40 W white light LED at R.T for 18 hours; and the large scale synthesis of 5,8-dimethyl-2-phenyl-3*a*,4,5,9*b*-tetrahydro-1*H*-pyrrolo[3,4-*c*]quinoline-1,3(2*H*)-dione.

with its highest photocatalytic activities. Although the EPR signals for $^1O_2$ could also be detected (Fig. 3f), no effect was observed for the photocatalysis. All these results demonstrate that $^{\bullet}O_2^-$ is the main intermediate to facilitate the cycloaddition reaction of *N*,*N*,4-trimethylaniline and 1-phenylpyrrolidine-2,5-dione.

With the excellent photocatalytic performance of HIAM-0030 toward the cycloaddition reaction of *N*,*N*,4-trimethylaniline and 1-phenylpyrrolidine-2,5-dione, we extended the substrates to five different *N*,*N*-dimethylanilines and five different maleimides to examine the feasibility of HIAM-0030 as a heterogeneous photocatalyst under the optimal photocatalytic conditions. As shown in Fig. 4, at least 90% conversions were obtained for all substrates regardless of their differences in the electron-donating or electron-withdrawing effects on the molecular skeleton of *N*,*N*-dimethylanilines or maleimides. The synthesized products were further confirmed by NMR spectra (Fig. S13–S22). Furthermore, a gram scale synthesis of 5,8-dimethyl-2-phenyl-3*a*,4,5,9*b*-tetrahydro-1*H*-pyrrolo[3,4-*c*]quinoline-1,3(2*H*)-dione was conducted, in which 7.50 mmol *N*,*N*,4-trimethylaniline, 3.75 mmol 1-phenylpyrrolidine-2,5-dione, 20.0 mg HIAM-0030 and 20.0 mL DMF were used under air with the irradiation of a 40 W white light LED for 18 hours. As expected, 1.0714 g target compound was obtained with 93% yield after purification using flash column chromatography. These results indicate that HIAM-0030 indeed can be used as an excellent photocatalyst to realize the highly efficient cycloaddition reaction of *N*,*N*-dimethylanilines and maleimides.

Conclusion

In conclusion, under the guidance of reticular chemistry, we have demonstrated the construction of four Olympic rings-inspired 2D-COFs, HIAM-0028 to HIAM-0031, using hexatopic aldehydes and diamine-based building units through a $C_6 + C_2$ approach. The suitable electronic structures and ability to generate reactive oxygen species endow these four COFs with the potential to serve as heterogeneous photocatalysts for the cycloaddition reaction of tertiary anilines and maleimides. Benefiting from the lower exciton binding energy, efficient separation and migration of electron–hole pairs, HIAM-0030 exhibits the highest photocatalytic activity (yields >90% for 10 substrates) even at the gram scale. The successful implementation of reticular chemistry for preparing COFs with unique structures provides a new insight into the rational design and synthesis of new porous materials to realize on-demand structures, properties and applications.

Author contributions

X.-Y. L. conceived the idea and designed the experiment; Z.-Y. Wang, C.-Q. Han, J.-X. Guo and S. Sun carried out the synthesis, characterization and photocatalysis of all materials. X.-Y. L., Z.-Y. Wang and C.-Q. Han wrote the manuscript with the help of all authors.

Conflicts of interest

The authors declare no competing financial interests.

Data availability

The data that support the findings of this study are available from the corresponding author, upon reasonable request.

Supplementary information: Materials, synthesis and characterization studies of COFs. See DOI: **https://doi.org/10.1039/d5sc03939h**.

Acknowledgements

X.-Y. Liu acknowledges the financial support from Shenzhen Polytechnic University. The term “Olympic” and the Olympic Symbol have been reproduced with the authorization of the International Olympic Committee.

References

1 H. Furukawa, K. E. Cordova, M. O'Keeffe and O. M. Yaghi, *Science*, 2013, **341**, 1230444.
2 C. S. Diercks and O. M. Yaghi, *Science*, 2017, 355.
3 S. Y. Ding and W. Wang, *Chem. Soc. Rev.*, 2013, **42**, 548–568.
4 K. T. Tan, S. Ghosh, Z. Wang, F. Wen, D. Rodríguez-San-Miguel, J. Feng, N. Huang, W. Wang, F. Zamora, X. Feng, A. Thomas and D. Jiang, *Nat. Rev. Methods Primers*, 2023, **3**, 1.
5 Z. Wang, S. Zhang, Y. Chen, Z. Zhang and S. Ma, *Chem. Soc. Rev.*, 2020, **49**, 708–735.
6 F. Xie, L. Yu, H. Wang and J. Li, *Angew. Chem., Int. Ed.*, 2023, **62**, e202300722.
7 L. Qin, C. Ma, J. Zhang and T. Zhou, *Adv. Funct. Mater.*, 2024, 2401562.
8 Y.-N. Gong, X. Guan and H.-L. Jiang, *Coord. Chem. Rev.*, 2023, **475**, 214889.
9 K.-Y. Wang, J. Zhang, Y.-C. Hsu, H. Lin, Z. Han, J. Pang, Z. Yang, R.-R. Liang, W. Shi and H.-C. Zhou, *Chem. Rev.*, 2023, **123**, 5347–5420.
10 A. Bavykina, N. Kolobov, I. S. Khan, J. A. Bau, A. Ramirez and J. Gascon, *Chem. Rev.*, 2020, **120**, 8468–8535.
11 A. Wang, M. Walden, R. Ettlinger, F. Kiessling, J. J. Gassensmith, T. Lammers, S. Wuttke and Q. Peña, *Adv. Funct. Mater.*, 2024, **34**, 2308589.
12 J. Ma, T. Shu, Y. Sun, X. Zhou, C. Ren, L. Su and X. Zhang, *Small*, 2022, **18**, 2103516.
13 J. Yang and Y. W. Yang, *Small*, 2020, **16**, e1906846.
14 O. M. Yaghi, M. O'Keeffe, N. W. Ockwig, H. K. Chae, M. Eddaoudi and J. Kim, *Nature*, 2003, **423**, 705–714.
15 N. W. Ockwig, O. Delgado-Friedrichs, M. O'Keeffe and O. M. Yaghi, *Acc. Chem. Res.*, 2005, **38**, 176–182.
16 O. M. Yaghi, M. J. Kalmutzki and C. S. Diercks, *Introduction to Reticular Chemistry*, Wiley, 2019, pp. 1–509.
17 M. O'Keeffe, M. A. Peskov, S. J. Ramsden and O. M. Yaghi, *Acc. Chem. Res.*, 2008, **41**, 1782–1789.
18 Z. Chen, S. L. Hanna, L. R. Redfern, D. Alezi, T. Islamoglu and O. K. Farha, *Coord. Chem. Rev.*, 2019, **386**, 32–49.

19 Y. Liu, M. O'Keeffe, M. M. J. Treacy and O. M. Yaghi, *Chem. Soc. Rev.*, 2018, **47**, 4642–4664.
20 Z. Chen, H. Jiang, M. Li, M. O'Keeffe and M. Eddaoudi, *Chem. Rev.*, 2020, **120**, 8039–8065.
21 L. Feng, K.-Y. Wang, X.-L. Lv, T.-H. Yan, J.-R. Li and H.-C. Zhou, *J. Am. Chem. Soc.*, 2020, **142**, 3069–3076.
22 R. Freund, S. Canossa, S. M. Cohen, W. Yan, H. Deng, V. Guillerm, M. Eddaoudi, D. G. Madden, D. Fairen-Jimenez, H. Lyu, L. K. Macreadie, Z. Ji, Y. Zhang, B. Wang, F. Haase, C. Wöll, O. Zaremba, J. Andreo, S. Wuttke and C. S. Diercks, *Angew. Chem., Int. Ed.*, 2021, **60**, 23946–23974.
23 N. R. Catarineu, A. Schoedel, P. Urban, M. B. Morla, C. A. Trickett and O. M. Yaghi, *J. Am. Chem. Soc.*, 2016, **138**, 10826–10829.
24 Z. Chen, Ł. J. Weseliński, K. Adil, Y. Belmabkhout, A. Shkurenko, H. Jiang, P. M. Bhatt, V. Guillerm, E. Dauzon, D.-X. Xue, M. O'Keeffe and M. Eddaoudi, *J. Am. Chem. Soc.*, 2017, **139**, 3265–3274.
25 V. Guillerm, T. Grancha, I. Imaz, J. Juanhuix and D. Maspoch, *J. Am. Chem. Soc.*, 2018, **140**, 10153–10157.
26 Z. Chen, Z. Thiam, A. Shkurenko, L. J. Weselinski, K. Adil, H. Jiang, D. Alezi, A. H. Assen, M. O'Keeffe and M. Eddaoudi, *J. Am. Chem. Soc.*, 2019, **141**, 20480–20489.
27 Y.-F. Zhang, Z.-H. Zhang, L. Ritter, H. Fang, Q. Wang, B. Space, Y.-B. Zhang, D.-X. Xue and J. Bai, *J. Am. Chem. Soc.*, 2021, **143**, 12202–12211.
28 J. Si, H.-L. Xia, K. Zhou, J. Li, K. Xing, J. Miao, J. Zhang, H. Wang, L.-L. Qu, X.-Y. Liu and J. Li, *J. Am. Chem. Soc.*, 2022, **144**, 22170–22177.
29 P.-H. Fang, K. Xing, L.-L. Qu, Z.-S. Ma, K. Zhou and X.-Y. Liu, *Small*, 2024, **20**, 2405540.
30 C.-Q. Han, L. Wang, J. Si, K. Zhou and X.-Y. Liu, *Small*, 2024, **20**, 2402263.
31 T.-T. Ma, G.-Z. Huang, X.-H. Wang, Y. Liang, R.-H. Li, B. Wang, S.-J. Yao, J.-P. Liao, S.-L. Li, Y. Yan and Y.-Q. Lan, *Natl. Sci. Rev.*, 2024, **11**, nwae177.
32 P.-J. Tian, X.-H. Han, Q.-Y. Qi and X. Zhao, *Chem. Sci.*, 2024, **15**, 9669–9675.
33 F. Wen, K. Xu, Y. Feng and N. Huang, *J. Am. Chem. Soc.*, 2024, **146**, 19680–19685.
34 Y. Liu, L. Yuan, W. Chi, W.-K. Han, J. Zhang, H. Pang, Z. Wang and Z.-G. Gu, *Nat. Commun.*, 2024, **15**, 7150.
35 T. Peng, C.-Q. Han, H.-L. Xia, K. Zhou, J. Zhang, J. Si, L. Wang, J. Miao, F.-A. Guo, H. Wang, L.-L. Qu, G. Xu, J. Li and X.-Y. Liu, *Chem. Sci.*, 2024, **15**, 3174–3181.
36 Z. Chen, P. Li, X. Zhang, P. Li, M. C. Wasson, T. Islamoglu, J. F. Stoddart and O. K. Farha, *J. Am. Chem. Soc.*, 2019, **141**, 2900–2905.
37 C. S. Diercks, Y. Liu, K. E. Cordova and O. M. Yaghi, *Nat. Mater.*, 2018, **17**, 301–307.
38 Z. Chen, P. Li, R. Anderson, X. Wang, X. Zhang, L. Robison, L. R. Redfern, S. Moribe, T. Islamoglu, D. A. Gómez-Gualdrón, T. Yildirim, J. F. Stoddart and O. K. Farha, *Science*, 2020, **368**, 297–303.
39 He, X.-J. Kong, J. Zhou, C. Zhao, K. Wang, X.-Q. Wu, X.-L. Lv, G.-R. Si, J.-R. Li and Z.-R. Nie, *J. Am. Chem. Soc.*, 2021, **143**, 9901–9911.
40 W.-K. Han, W. Yuan, Z.-G. Gu and Y. Zhao, *ACS Materials Lett.*, 2024, **6**, 2276–2294.
41 Y. Chen and D. Jiang, *Acc. Chem. Res.*, 2024, **57**(21), 3182–3193.
42 A. Alam, B. Kumbhakar, A. Chakraborty, B. Mishra, S. Ghosh, A. Thomas and P. Pachfule, *ACS Materials Lett.*, 2024, **6**, 2007–2049.
43 A. Rodríguez-Camargo, K. Endo and B. V. Lotsch, *Angew. Chem., Int. Ed.*, 2024, **63**, e202413096.
44 B. Mishra, A. Alam, A. Chakraborty, B. Kumbhakar, S. Ghosh, P. Pachfule and A. Thomas, *Adv. Mater.*, 2025, 2413118.
45 P. F. Wei, M. Z. Qi, Z. P. Wang, S. Y. Ding, W. Yu, Q. Liu, L. K. Wang, H. Z. Wang, W. K. An and W. Wang, *J. Am. Chem. Soc.*, 2018, **140**, 4623–4631.
46 Q. Li, X. Lan, G. An, L. Ricardez-Sandoval, Z. Wang and G. Bai, *ACS Catal.*, 2020, **10**, 6664–6675.
47 S. Li, L. Li, Y. Li, L. Dai, C. Liu, Y. Liu, J. Li, J. Lv, P. Li and B. Wang, *ACS Catal.*, 2020, **10**, 8717–8726.
48 A. Basak, S. Karak and R. Banerjee, *J. Am. Chem. Soc.*, 2023, **145**, 7592–7599.
49 H. Pang, G. Liu, D. Huang, Y. Zhu, X. Zhao, W. Wang and Y. Xiang, *Angew. Chem., Int. Ed.*, 2023, **62**, e202313520.
50 S. Li, W. Wei, K. Chi, C. T. J. Ferguson, Y. Zhao and K. A. I. Zhang, *J. Am. Chem. Soc.*, 2024, **146**, 12386–12394.
51 L.-B. Xing, K. Cheng, H. Li, K. Niu, T.-X. Luan, S. Kong, W. W. Yu, P.-Z. Li and Y. Zhao, *Angew. Chem., Int. Ed.*, 2025, **64**, e202425668.
52 F. Jin, E. Lin, T. Wang, D. Yan, Y. Yang, Y. Chen, P. Cheng and Z. Zhang, *Chem*, 2022, **8**, 3064–3080.
53 C. Wu, X. Li, M. Shao, J. Kan, G. Wang, Y. Geng and Y.-B. Dong, *Chin. Chem. Lett.*, 2022, **33**, 4559–4562.
54 Z. Almansaf, J. Hu, F. Zanca, H. R. Shahsavari, B. Kampmeyer, M. Tsuji, K. Maity, V. Lomonte, Y. Ha, P. Mastrorilli, S. Todisco, M. Benamara, R. Oktavian, A. Mirjafari, P. Z. Moghadam, A. R. Khosropour and H. Beyzavi, *ACS Appl. Mater. Interfaces*, 2021, **13**, 6349–6358.
55 Y. Zhao, K. Zhang, K. Zhu, Y. Zhao, H. Zhai and J. Qiu, *Green Chem.*, 2024, **26**, 2645–2652.
56 J.-J. Li, J.-Y. Liu, S.-Y. Gao, X. Yang and R. Cao, *J. Am. Chem. Soc.*, 2025, **147**, 21754–21763.